

1 **Modulation of galactic cosmic rays during the**  
2 **unusual solar minimum between cycles 23 and 24**

L.-L. Zhao<sup>1</sup>, G. Qin<sup>1</sup>, M. Zhang<sup>2</sup>, and B. Heber<sup>3</sup>

arXiv:1310.7076v2 [astro-ph.SR] 22 Jan 2014

---

L.-L. Zhao, State Key Laboratory of Space Weather, National Space Science Center, Chinese Academy of Sciences, P.O. Box 8701, Beijing 100190, China, (llzhao@spaceweather.ac.cn)

G. Qin, State Key Laboratory of Space Weather, National Space Science Center, Chinese Academy of Sciences, P.O. Box 8701, Beijing 100190, China, (gqin@spaceweather.ac.cn)

M. Zhang, Department of Physics and Space Science, Florida Institute of Technology, Melbourne, FL 32901, USA., (mzhang@fit.edu)

B. Heber, Institut für Experimentelle und Angewandte Physik, Christian-Albrechts-Universität zu Kiel, 24118 Kiel, Germany, (heber@physik.uni-kiel.de)

<sup>1</sup>State Key Laboratory of Space Weather,

3 **Abstract.** During the recent solar minimum between cycles 23 and 24  
4 (solar minimum  $P_{23/24}$ ) the intensity of Galactic Cosmic Rays (GCRs) mea-  
5 sured at the Earth was the highest ever recorded since space age. It is the  
6 purpose of this paper to resolve the most plausible mechanism for this un-  
7 usually high intensity. A GCR transport model in three-dimensional helio-  
8 sphere based on a simulation of Markov stochastic process is used to find the  
9 relation of cosmic ray modulation to various transport parameters, includ-  
10 ing solar wind (SW) speed, distance of heliospheric boundary, magnitude of  
11 interplanetary magnetic field (IMF) at the Earth, tilt angle of heliospheric  
12 current sheet (HCS), values of parallel and perpendicular diffusion coefficients.  
13 We calculate GCR proton energy spectra at the Earth for the last three so-  
14 lar minima  $P_{21/22}$ ,  $P_{22/23}$ , and  $P_{23/24}$ , with the transport parameters obtained

---

National Space Science Center, Chinese

Academy of Sciences, Beijing 100190, China

<sup>2</sup>Department of Physics and Space

Science, Florida Institute of Technology,

Melbourne, FL 32901, USA

<sup>3</sup>Institut für Experimentelle und

Angewandte Physik,

Christian-Albrechts-Universität zu Kiel,

24118 Kiel, Germany

15 from observations. Besides weak IMF magnitude and slow SW speed, we find  
16 that a possible low magnetic turbulence, which increases the parallel diffu-  
17 sion and reduces the perpendicular diffusion in the polar direction, might be  
18 an additional possible mechanism for the high GCR intensity in the solar min-  
19 imum  $P_{23/24}$ .

## 1. Introduction

Galactic Cosmic Rays (GCRs) are energetic charged particles originated far away from the heliosphere. The high energy GCRs may reach the Earth atmosphere to produce secondary elementary particles that can be measured by ground-based Neutron Monitors (NMs) or other detectors. Although the lower energy GCRs (tens of MeV/nuc) are not usually detected by the ground-based NMs, they can be measured in space by spacecraft except during solar energetic particle (SEP) events produced by solar flares or coronal mass ejections. Unlike SEPs, GCRs form a nearly stable and isotropic background of high-energy radiation. The intensity of GCRs is slowly modulated in an anti-correlation [McDonald, 1998] with the solar activity level of 11-year cycle. It occurs because GCR particles have to travel through the magnetized interplanetary medium. The interplanetary magnetic field emanated from the Sun changes with the solar cycle, causing variations in the speed of particle transport processes such as diffusion, convection, adiabatic deceleration and drifts. Therefore, GCRs can provide important information about their propagation and modulation mechanisms in the heliosphere [Kóta, 2013]. Once the level of modulation is figured out, we can reconstruct the spectrum and composition of GCRs in the interstellar space, which can further provide information about their origin and the acceleration mechanism that produces them at the source.

The GCRs intensity measured at the Earth reached a record high level during the last solar minimum between cycles 23 and 24, noted as solar minimum  $P_{23/24}$  from now on. Figure 1 shows the GCR count rates as measured by the Apatity NM, whose effective cutoff rigidity is 0.65 GV, and the monthly averaged SunSpot Numbers (SSNs) for the past

41 forty years. The red dashed-lines indicate the epochs of solar minima, which demarcate  
42 the solar cycles represented by the red numbers from the next ones. The black dashed-  
43 lines indicate the epochs of solar maxima, which demarcate the periods of solar magnetic  
44 polarity represented by ‘ $A > 0$ ’ or ‘ $A < 0$ ’. From Figure 1 we can clearly see a few  
45 well-known features of GCRs. First, an anti-correlation between GCR intensity and 11-  
46 year solar activity cycles is shown. Second, in the cycles with  $A < 0$  magnetic polarity  
47 like 1980s, and 2000s, when the Interplanetary Magnetic Field (IMF) points towards  
48 (outwards) the Sun in the northern (southern) hemisphere [Scherer et al., 2004], the time  
49 profiles of positively charged particles in the GCR are peaked, whereas the time profile  
50 is more or less flat in the cycle of  $A > 0$  magnetic polarity like 1970s and 1990s. This  
51 phenomenon is attributed to the “waviness” of the Heliospheric Current Sheet (HCS) [see  
52 Kóta and Jokipii, 1983]. Besides the above characteristic behavior, we can also notice  
53 that the monthly mean SSN reached a minimum value around 2009. It was followed by a  
54 high GCR count rate which breaks the previous record February 1987 level. Meanwhile,  
55 the Solar Wind (SW) density, pressure, and IMF strength all reached the lowest values  
56 ever observed during the latest measurements made by Ulysses [Heber et al., 2009].

57 Various models, empirical and theoretical [e.g., Ahluwalia et al., 2010; Manuel et al.,  
58 2011], have been used to study the unusual GCRs intensities during this solar minimum.  
59 The empirical and phenomenological GCRs modulation models are derived from observa-  
60 tions without considering the physical processes [e.g., Nymmik et al., 1992; Zhao and Qin,  
61 2013]. But in order to understand the physical causes for such phenomenon, one needs to  
62 use theoretical models for GCR modulation. The most successful ones are based on Parker  
63 [1965], which essentially includes all important GCR modulation mechanisms such as out-

ward convection by the SW, diffusion through the irregular IMF, gradient and curvature drifts, adiabatic deceleration from the divergence of the expanding SW. Burger and Potgieter [1989] further concluded that GCR drift in the tilted HCS can be an important effect in solar modulation of GCR. The variation of particle perpendicular diffusion through the changes in magnetic field turbulence may also cause different levels of modulation. Recent studies also show that there is remarkable modulation in the outer heliosphere [Scherer et al., 2011], probably as well as beyond the heliopause [Strauss et al., 2013; Strauss and Potgieter, 2014]. Therefore, the GCR intensities measured at Earth is a comprehensive result of these different conditions for particle propagation through the heliosphere. More detailed theories were summarized in review papers such as Potgieter [1998], Jokipii and Kóta [2000], Heber et al. [2006] and Potgieter [2013]. Finite-difference method [Jokipii and Kopriva, 1979; Kóta and Jokipii, 1983] and stochastic method [Zhang, 1999; Ball et al., 2005; Pei et al., 2010] have been used to solve the 2-D or 3-D Parker's transport equation for GCR modulation. Calculation results were able to reproduce many observed features from measurements by spacecraft, balloon experiments, and NMs. Although the study of GCR modulation has been progressed significantly, much work still need to be done. The record level of GCR intensity during the last solar minimum naturally throw us a question: what causes the unusual solar minimum?

It is the purpose of this paper to answer the question of what causes the unusually high GCR intensity at Earth in the last solar minimum. We first present the observations of SW and IMF parameters measured at 1 AU for the last several solar cycles. Next we use a GCR transport model with numerical simulation to study the modulation of cosmic rays. Finally, through comparing our simulation results with the observations, we show what

87 are the possible reasons for the unusual high GCR intensity for the last solar minimum  
88  $P_{23/24}$ .

## 2. Modulation Model

89 The distribution function of cosmic rays propagating through the heliosphere is governed  
90 by Parker transport equation [Parker, 1965],

$$\frac{\partial f}{\partial t} = \nabla \cdot (\kappa \cdot \nabla f) - (\mathbf{V}_{sw} + \mathbf{V}_d) \cdot \nabla f + \frac{p}{3} (\nabla \cdot \mathbf{V}_{sw}) \frac{\partial f}{\partial p}, \quad (1)$$

91 where  $f(\mathbf{r}, p)$  is the cosmic ray distribution function, with  $p$  the particle's momentum,  $\mathbf{r}$   
92 the particle's position,  $\mathbf{V}_{sw}$  the SW speed, and  $\mathbf{V}_d$  the gradient and curvature drifts in  
93 the IMF. The spatial diffusion coefficient tensor  $\kappa$  is diagonal, and consists of a parallel  
94 diffusion coefficient  $\kappa_{\parallel}$  and two perpendicular diffusion coefficients,  $\kappa_{\perp r}$  the perpendicular  
95 diffusion coefficient in the radial direction and  $\kappa_{\perp \theta}$  that in the polar direction. Here we  
96 assume the parameters are axially symmetric and time-independent on the time scale  
97 of average particle transport through the heliosphere as discussed below. In addition,  
98 we assume the IMF as a Parker spiral, and that the SW velocity is radial from the sun  
99 and constant in magnitude. Note that cosmic ray is considered isotropic, otherwise the  
100 adiabatic deceleration term, the last one in the right hand side of equation (1), has to be  
101 in the anisotropic form [e.g., Qin et al., 2004].

102 In this work a relatively simple spatial and momentum dependence of the diffusion  
103 coefficients is assumed following Zhang [1999] and Ferreira et al. [2001]. Firstly, parallel  
104 diffusion is set as [Zhang, 1999; Ferreira et al., 2001]

$$\kappa_{\parallel} = d\kappa_0\beta \left(\frac{p}{p_0}\right)^{\gamma} \left(\frac{B_e}{B}\right)^{\eta}, \quad (2)$$

with the parallel diffusion factor  $d$  being an adjustable constant,  $\kappa_0 = 1 \times 10^{22} \text{ cm}^2 \text{ s}^{-1}$ ,  $\gamma = 1/3$ ,  $\eta = 1$ ,  $\beta$  is a fraction of particle's speed relative to the speed of light,  $p_0 = 1 \text{ GeV c}^{-1}$  is a reference momentum,  $B_e$  is the magnetic field strength at the Earth, and  $B$  is the magnetic field at the location of the particle. Note that we set  $\gamma = 1/3$  according to QLT of cosmic rays [Jokipii, 1966] for a Kolmogorov turbulence spectrum. However, other parameter from a Kraichnans scaling could also be used. Note that the form of diffusion coefficient for cosmic ray propagation in the heliosphere is rather complicated [e.g., Matthaeus et al., 2003; Qin, 2007; Shalchi et al., 2004; Zank et al., 2004]. For example, it is assumed that a break in the rigidity-dependent parallel diffusion coefficient around 4 GV is necessary for explaining the observed boron-to-carbon ratio [Büsching and Potgieter, 2008; Shalchi and Büsching, 2010]. In this work we use diffusion forms without break for the simplicity purpose. Since the peak of GCR spectrum at solar minimum is well below 1 GeV and the level of modulation is much lower for  $> 4 \text{ GV}$  GCR, the effect of the break on modulated spectrum is insignificant. Secondly, the diffusion coefficients in the two perpendicular directions are set to proportional to the parallel diffusion coefficient according to test particle simulations [e.g., Giacalone and Jokipii, 1999; Qin, 2002, 2007],

$$\kappa_{\perp r} = a\kappa_{\parallel}/d = a\kappa_0\beta \left(\frac{p}{p_0}\right)^{\gamma} \left(\frac{B_e}{B}\right)^{\eta}, \quad (3)$$

with an adjustable constant factor  $a$  for the radial perpendicular diffusion, and

$$\kappa_{\perp \theta} = b\kappa_{\parallel}/d = b\kappa_0\beta \left(\frac{p}{p_0}\right)^{\gamma} \left(\frac{B_e}{B}\right)^{\eta}, \quad (4)$$

with an adjustable constant factor  $b$  for the polar diffusion perpendicular diffusion. Here, we assume different values of the parameters  $a$  and  $b$  for non-axisymmetric perpendicular diffusion because of non-axisymmetry of turbulence [e.g., Matthaeus et al., 2003] or the

125 background magnetic field. Note that Effenberger et al. [2012a] also discussed the effects  
 126 of different perpendicular diffusion coefficients.

127 We also include a wavy HCS provided by Jokipii and Thomas [1981], who showed that  
 128 if the solar wind velocity is radial and constant in magnitude, the HCS can be represented  
 129 by

$$\theta' = \frac{\pi}{2} + \sin^{-1} \left[ \sin \alpha \sin \left( \phi - \phi_0 + \frac{r\Omega}{V_{sw}} \right) \right], \quad (5)$$

130 where  $\alpha$  is the HCS tilt angle (TA),  $\phi_0$  is an arbitrary azimuthal phase constant, and  
 131  $\Omega$  is the angular velocity of the Sun's rotation corresponding to a period of 27.27 days.  
 132 Furthermore, if the TA  $\alpha \ll 1$ , the HCS can be approximately written as

$$\theta' \approx \frac{\pi}{2} + \alpha \sin \left( \phi - \phi_0 + \frac{r\Omega}{V_{sw}} \right). \quad (6)$$

133 Next, using the approximate form of HCS equation (6) we can express the Parker's spiral  
 134 IMF as,

$$\mathbf{B} = \frac{A}{r^2} \left( \hat{\mathbf{e}}_r - \frac{r\Omega \sin \theta}{V_{sw}} \hat{\mathbf{e}}_\phi \right) \left[ 1 - 2H(\theta - \theta') \right], \quad (7)$$

135 where  $A$  is used to determine the strength and polarity of IMF, with pointing either  
 136 outward ( $A > 0$ ) or inward ( $A < 0$ ) in the northern hemisphere. The Heaviside step  
 137 function  $H$  is used to switch the field's direction across the HCS at  $\theta = \theta'$ . Note that a  
 138 Fisk field with latitude-dependent solar wind speed should be used in 3D modeling, but  
 139 Hitge and Burger [2010] found that the solar wind speed does not significantly influence  
 140 cosmic ray transport in most conditions. Therefore, for the simplicity purpose, here we  
 141 use Parker field with constant solar wind speed.

142 We describe drifts in the IMF in two different ways following Burger and Potgieter  
 143 [1989]. Particles whose gyro motion do not cross the HCS have a pitch-angle averaged  
 144 drift velocity given by the guiding center approximation. Derived with equation (7), the

regular drift velocity of a particle with charge  $q$ , momentum  $p$ , and speed  $v$  can be written  
as

$$\begin{aligned} \mathbf{V}_{dr} &= \frac{pv}{3q} \nabla \times \left( \frac{\mathbf{B}}{B^2} \right) \\ &= \frac{2pvr}{3qA(1 + \Gamma^2)^2} \left[ -\frac{\Gamma}{\tan \theta} \hat{\mathbf{e}}_r + (2 + \Gamma^2)\Gamma \hat{\mathbf{e}}_\theta + \frac{\Gamma^2}{\tan \theta} \hat{\mathbf{e}}_\phi \right], \end{aligned} \quad (8)$$

where  $\Gamma = r\Omega \sin \theta / V_{sw}$  is the tangent of the angle between the direction of IMF and the radial direction  $\hat{\mathbf{e}}_r$ . Particles with a trajectory that crosses the HCS will experience a fast meandering drift along the HCS. Assuming a locally flat HCS, the magnitude of the drift velocity  $v_{ns}$  along the HCS can be approximated as [see also Burger and Potgieter, 1989]

$$v_{ns} = \left\{ 0.457 - 0.412 \frac{d}{r_L} + 0.0915 \left( \frac{d}{r_L} \right)^2 \right\} v, \quad \text{for } |d| < 2r_L \quad (9)$$

where  $d$  is the distance from the position of the particle to the HCS,  $r_L$  is gyroradius, and  $v$  is the particle speed. Calculation results with this realistic HCS drift is the same as those with analytical HCS drift of Kóta and Jokipii [1983]. The direction of the HCS drift velocity is parallel to the HCS and perpendicular to the HMF ([e.g. Burger and Potgieter, 1989]). See Burger [2012] for detailed discussion on the drift velocity direction in 3-D HCS. Note that both the drift expressions (equation (8) and (9)) are only valid when scattering is neglected, which is the case for solar minimum.

The inner boundary is set at  $r = 0.3$  AU as an absorption boundary. The outer boundary of the heliosphere, which assumed as the heliopause (HP) at  $r = R_{HP}$ , is set to be a GCR source with an assumed local interstellar spectrum (LIS)

$$J_{LIS} \propto p(m_0^2 c^2 + p^2)^{-1.8} \quad (10)$$

by following Zhang [1999]. Though it is believed that with measurements from Voyager 1 spacecraft in the vicinity of the heliopause [Decker et al., 2012] and highly accurate mea-

163 surements by the PAMELA mission [Adriani et al., 2011], it is now possible to determine  
164 the lower limit of the very LIS for protons, helium and other ions with numerical simula-  
165 tions [Herbst et al., 2012]. Nevertheless, the true LIS is still far from conclusive [Webber  
166 et al., 2013]. In addition, different LIS models can produce the observed spectrum with  
167 LIS model-dependent modulation parameters [Herbst et al., 2010]. Furthermore, recent  
168 studies show that remarkable modulation exists in the outer heliosphere and even beyond  
169 the heliopause [e.g. Scherer et al., 2011; Strauss et al., 2013]. And the outer heliospheric  
170 structure and boundary of the dynamic heliosphere also change associated with the vary-  
171 ing solar activity [Zank and Müller, 2003; Scherer and Fahr, 2003; Pogorelov et al., 2009].  
172 However, assuming a steady LIS during the studied period, a distance of the boundary,  
173 and an inclusion of the heliosheath just has minor effects for modulation at 1 AU, since  
174 most of the energy loss occurs in the inner heliosphere. Here we study the modulation pro-  
175 cess within the inner heliosphere, so only the LIS without other effects over the boundary  
176 is considered for simplicity purpose.

### 3. Interplanetary Environment

177 In order to understand solar modulation of GCR with model simulations using the  
178 transport equation (1), it is important to use appropriate particle transport parameters,  
179 which are determined by the properties of the solar wind, heliospheric magnetic field,  
180 and energetic particles. Figure 2 shows the temporal evolution of IMF  $B_e$  and SW speed  
181  $V_{sw}$ , both of which are measured at 1 AU, and the HCS TA  $\alpha$ , for the last three solar  
182 cycles. The IMF and the SW velocity data are obtained by averaging the OMNI data  
183 over one-month intervals. And the TA of the HCS data are obtained from the WSO Web  
184 site with the “new” model. In Figure 2, we illustrate the three epochs of solar minima in

185 grey shadows of about half a year long as  $P_{21/22}$  (1986, 91 - 1986, 273),  $P_{22/23}$  (1996, 1  
 186 - 1996, 182), and  $P_{23/24}$  (2009, 121 - 2009, 304). Note that all the data during the solar  
 187 minima in this work are averaged over the periods shown above. From Figure 2 we can  
 188 see that both the magnitude of IMF and the SW speed are very low during the recent  
 189 solar minimum  $P_{23/24}$ , but the TA of HCS is not at the lowest level.

190 The solar magnetic polarity and the half-year average of  $V_{sw}$ ,  $B_e$ , and  $\alpha$  during the three  
 191 solar minima, which are used in our simulations for GCR modulation, are shown in the  
 192 Table 1.

#### 4. Numerical Methods

193 There are many approximate solutions of the Parker equation available, e.g. the most  
 194 generally used force field solution [Moraal, 2013]. The appeal of the force field approach  
 195 lies in the fact that observed modulation can be described with a single parameter termed  
 196 modulation potential  $\phi$  [Caballero-Lopez and Moraal, 2004]. The model assume an equi-  
 197 librium between diffusion and adiabatic energy loss. Effects of drift and convection are  
 198 neglected. While it is possible to reproduce the observed GCR modulation in the inner  
 199 heliosphere through adjusting the modulation potential  $\phi$  using the force field model, it  
 200 cannot resolve the contribution from distinct physical mechanisms.

201 In this work, we use the time-backward Markov stochastic process method proposed by  
 202 Zhang [1999] to solve the Parker transport equation in 3-D spherical coordinate (1). As  
 203 it is more versatile and less computationally intensive, this method has been successfully  
 204 implemented with different cosmic ray transport models, such as Qin et al. [2005] and Ball  
 205 et al. [2005]. In this method, we trace virtual particles from the observation point back  
 206 to the outer boundary with the interstellar flux expressed as equation (10). Note that the

207 GCR protons distribution is written as  $j \sim p^2 f$ . The set of SDEs, being equivalent to  
 208 equation (1), for a pseudo-particle in position  $(r, \theta, \phi)$  and momentum  $p$  using spherical  
 209 coordinate can be written as equation (11) [see also Pei et al., 2010; Strauss et al., 2012].  
 210 Kopp et al. [2012] and Effenberger et al. [2012b] also present a general discussion on the  
 211 SDE technique for solving Parker transport equation.

$$\begin{aligned}
 dr &= \left[ \frac{1}{r^2} \frac{\partial}{\partial r} (r^2 \kappa_{rr}) + \frac{1}{r \sin \theta} \frac{\partial \kappa_{r\phi}}{\partial \phi} - V_{sw} - v_{dr} \right] ds \\
 &\quad + \sqrt{2\kappa_{rr} - \frac{2\kappa_{r\phi}^2}{\kappa_{\phi\phi}}} dW_r + \frac{\sqrt{2}\kappa_{r\phi}}{\sqrt{\kappa_{\phi\phi}}} dW_\phi, \\
 d\theta &= \left[ \frac{1}{r^2 \sin \theta} \frac{\partial}{\partial \theta} (\sin \theta \kappa_{\theta\theta}) - \frac{v_{d\theta}}{r} \right] ds + \frac{\sqrt{2\kappa_{\theta\theta}}}{r} dW_\theta, \\
 d\phi &= \left[ \frac{1}{r^2 \sin^2 \theta} \frac{\partial \kappa_{\phi\phi}}{\partial \phi} + \frac{1}{r^2 \sin \theta} \frac{\partial}{\partial r} (r \kappa_{r\phi}) - \frac{v_{d\phi}}{r \sin \theta} \right] ds \\
 &\quad + \frac{\sqrt{2\kappa_{\phi\phi}}}{r \sin \theta} dW_\phi, \\
 dp &= \frac{p}{3r^2} \frac{\partial r^2 V_{sw}}{\partial r} ds.
 \end{aligned} \tag{11}$$

212 Using the stochastic simulation, we can obtain not only modulated GCRs fluxes, but also  
 213 the behavior of individual particle, e.g. the propagation time and energy loss [Strauss  
 214 et al., 2011]. In addition, we can incorporate almost any kind of magnetic field config-  
 215 uration according to observations or MHD numerical simulations [Strauss et al., 2013].  
 216 Furthermore, this stochastic numerical method is more computationally efficient than the  
 217 traditional finite difference approach, with the added advantage that it is easy to paral-  
 218 lelize. Note that the integration of stochastic differential equation is performed in terms  
 219 of spherical coordinates, which further enhances the computational efficiency by reducing  
 220 coordinate transformations.

## 5. Modulation Effects

221 In this section the effects of various transport parameters on GCR modulation are  
 222 discussed. Throughout this section, we set magnitude of IMF at 1 AU  $B_e = 5$  nT, SW  
 223 speed  $V_{sw} = 400$  km/s, TA of HCS  $\alpha = 0^\circ$ , and heliospheric outer boundary distance  
 224 as 80 AU, unless otherwise stated. Note that all results from numerical simulations and  
 225 observations are at 1 AU in the ecliptic.

### 5.1. Modulation Effects of Interplanetary Parameters

226 First, we study the modulation effects of interplanetary solar wind and magnetic field  
 227 parameters. In these simulations, we set diffusion factors  $a = 0.03$ ,  $b = 0.01$  and  $d = 1$   
 228 in equations (3), (4) and (2), respectively. The TA of HCS is set to  $\alpha = 0^\circ$  which is  
 229 appropriate for the solar minimum condition. Figure 3 illustrates separately the computed  
 230 differential intensity for GCR protons with different interplanetary parameters used in this  
 231 study. The calculations are done for both solar magnetic polarities. The top panels of  
 232 each figure show the results in the  $A > 0$  epochs, and the bottom panels show the results  
 233 in the  $A < 0$  epochs, with the interstellar unmodulated spectrum (grey lines) for reference.

234 Figure 3(a) shows the influence of different SW speeds on GCR proton intensity, with  
 235 the dark solid, dotted, and dashed lines representing three assumptions of SW speed,  
 236 300 km/s, 400 km/s, and 500 km/s, respectively. Although the IMF magnitude at the  
 237 Earth  $B_e$  is fixed, the magnetic field magnitude in the heliosphere is dependent on the  
 238 SW speed and varies according to equation (7). We can see there is an obvious anti-  
 239 correlation between SW speed and GCR intensity. Figure 3(b) illustrates the influence  
 240 of the heliospheric outer boundary radial distance on GCR intensity, with the dark solid,  
 241 dotted, and dashed lines representing three assumptions for the outer boundary radial

242 distance, 60 AU, 80 AU, and 100 AU, respectively. We can see that the outer boundary  
243 radial distance has little effect on the GCR flux measured at 1 AU, no matter whether  
244  $A > 0$  or  $A < 0$ . In Figure 3(c) the computed GCR proton intensities for different  
245 magnitude of IMF at 1 AU are shown. Compared with the results of SW speed and outer  
246 heliospheric boundary, the increased magnitude of IMF remarkably declines the GCR  
247 intensity for both magnetic epochs, especially for the lower energy range.

248 Overall, Figure 3 suggests that, in our model, the low SW speed and magnitude of  
249 IMF play significant role in increasing the GCR flux, while the effect of outer heliospheric  
250 boundary is negligible. Therefore, we set the outer heliospheric boundary distance as 80  
251 AU in the rest of the paper, but the SW speed and magnitude of IMF for each period  
252 according to the Table 1.

253 In order to show the effectiveness of lower SW speed and magnitude of IMF on the  
254 significant increase of GCR intensity in the recent extreme solar minimum, we calculate  
255 GCR intensities with interplanetary properties during each of the last three solar minima  
256 shown in Figure 4. Here, we set SW speed  $V_{sw}$  and IMF magnitude at the Earth  $B_e$   
257 during the last three solar minima as that in the Table 1. In Figure 4(a), by setting TA of  
258 HCS as 0, we find that the GCR intensity during  $P_{23/24}$  increases significantly. However,  
259 in Figure 4(b), by setting TA of HCS for different solar minima as shown in Table 1, the  
260 increase of the GCR intensity during  $P_{23/24}$  is less prominent compared with the spacecraft  
261 measurements shown later. Although the particle drifts, including the global gradient and  
262 curvature drifts, still play a significant role in CR modulation, the fact that the TA of  
263 HCS during  $P_{23/24}$  is not the lowest prevent us from reproducing the abnormally high

264 GCR intensity. So we need to consider the other physical mechanisms of modulation  
 265 processes.

## 5.2. Modulation Effects of Diffusion Coefficients

266 Since during the extreme solar minimum  $P_{23/24}$ , an  $A < 0$  epoch, the solar activity  
 267 was unusually quiet compared to that in the other solar minima, with an expected lower  
 268 turbulence level in solar wind, both the radial and polar perpendicular diffusion coeffi-  
 269 cients,  $\kappa_{\perp r}$  and  $\kappa_{\perp \theta}$ , respectively, became smaller, and the parallel diffusion coefficient,  
 270  $\kappa_{\parallel}$ , became larger. Here, we investigate the effects of polar perpendicular diffusion factor  
 271  $b$ , radial perpendicular diffusion factor  $a$ , and parallel diffusion factor  $d$ , on the GCR  
 272 intensity, especially during an  $A < 0$  epoch (Figure 5). It is similar to Reinecke and  
 273 Potgieter [1993] who discussed different diffusion coefficients on the different intensity of  
 274 CR during consecutive solar minimum. Following Effenberger et al. [2012a], we also use  
 275 an anisotropic diffusion coefficients in this study. In these simulations, we set diffusion  
 276 factors  $a = 0.03$ ,  $b = 0.01$  and  $d = 1$  in equations (3), (4) and (2), respectively, unless  
 277 otherwise stated.

278 The modulation effectiveness of  $\kappa_{\perp \theta}$  for both magnetic epochs,  $A > 0$  and  $A < 0$ , is  
 279 illustrated in Figure 5(a). Simulation results with  $b = 0.01$ ,  $b = 0.03$ , and  $b = 0.05$   
 280 are shown with dark solid, dotted, and dashed lines, respectively. While a lower polar  
 281 perpendicular diffusion factor  $b$  has little effect on the GCRs intensity in the  $A > 0$  epochs,  
 282 it can significantly increase GCRs intensity in the  $A < 0$  epochs. Moreover, Figure 5(b)  
 283 and 5(c) show that higher radial perpendicular diffusion factor  $a$  and parallel diffusion  
 284 factor  $d$  can increase GCRs intensity slightly for both solar epochs. Nevertheless, this

285 effect can be significantly weakened by an decrease of polar perpendicular diffusion factor  
 286  $b$ .

287 The above study shows that the decrease of  $b$  can cause the increase of GCR intensity.  
 288 In an  $A < 0$  epoch, this influence is more effective than the factor  $a$  and  $d$ . Therefore, it  
 289 is possible to use the combined effect of these transport parameters to explain the record  
 290 level of GCR flux in  $P_{23/24}$  solar minimum. Note that, in the following simulation, the  
 291 values of magnetic field magnitude  $B_e$ , solar wind speed  $V_{sw}$ , and tilt angle of current  
 292 sheet  $\alpha$  are from measurements, but the diffusion factors  $a$ ,  $b$ , and  $d$  are free parameters  
 293 constrained by fitting numerical simulation results to the spacecraft measurements.

## 6. GCRs Data

294 In this paper, we use GCRs data from both ground based NM count rates and proton  
 295 flux of spacecraft measurements. The GCR data are obtained with half-year average for  
 296 each of three solar minimum,  $P_{21/22}$ ,  $P_{22/23}$ , and  $P_{23/24}$ .

297 The NM stations we use for GCRs data are Apatity, Oulu, Yakutsk, Moscow, Novosi-  
 298 birsk, Lomnický štít, Jungfraujoch, Hermanus, Rome, Tbilisi, and Potchefstroom NMs.  
 299 In order to compare GCRs count rates measured by NMs with flux from simulation results,  
 300 we use the effective energy of each NM [Alanko et al., 2003], which can be approximated  
 301 as

$$E_{\text{eff}} = E_1 + \frac{E_2 (P_c/P_1)^{1.25}}{1 + 10 \exp(-0.45P_c/P_1)}, \quad (12)$$

302 where  $P_c$  is the local geomagnetic cutoff rigidity,  $E_1 = 6.4$  GeV,  $E_2 = 1.45$  GeV, and  
 303  $P_1 = 1$  GV. Thus the integral GCR flux above the effective energy  $M(E_{\text{eff}})$  is defined as

$$M(E_{\text{eff}}) = \int_{E_{\text{eff}}}^{\infty} j(E) d(E) \quad (13)$$

304 is directly proportional to the NM count rates, or

$$M(E_{\text{eff}}) = K_{\text{NM}}N(P_c), \quad (14)$$

305 with  $N(P_c)$  the NM count rates, and  $K_{\text{NM}}$  a constant for any NM. Therefore, for different  
 306 NMs we can compare the computed  $M(E_{\text{eff}})$  with observational data of the NM count  
 307 rates. Note that the effective energy is quite different from the median rigidity below  
 308 which lies 50% of detector counting rate [Ahluwalia and Fikani, 2007], widely used for  
 309 transient cosmic ray solar modulation studies [Ahluwalia et al., 2013].

310 Table 2 shows the local geomagnetic cutoff rigidity  $P_c$ , and the corresponding effective  
 311 energy  $E_{\text{eff}}$  of NMs used in our work.

312 The data are obtained from STEREO and PAMELA for energy 22 ~ 77 MeV and  
 313 82 ~ 20,000 MeV, respectively, during the period  $P_{23/24}$ , and IMP-8 for energy 70 ~ 400  
 314 MeV during the periods  $P_{21/22}$  and  $P_{22/23}$ . The data of IMP-8 and STEREO contain both  
 315 GCRs and SEPs. It is assumed that the modulated GCRs flux can be described as a stable  
 316 “background”, while SEPs appear typically as short spikes of a few days long except for  
 317 relative higher energy particles. Therefore, similar to what was done in Qin et al. [2012]  
 318 we use an automatic despiking algorithm based on Poincaré map thresholding method  
 319 [Goring and Nikora, 2002] to remove the SEP spikes for STEREO and IMP-8 data. For  
 320 more details to remove the SEP contamination in the time-series GCR flux from spacecraft  
 321 observations, please refer to Qin et al. [2012].

## 7. Simulation Results

322 In the following we compare the results of our numerical simulation of GCR spectra  
323 with measurements to find out possible reasons for the unusually high cosmic ray intensity  
324 during the  $P_{23/24}$  solar minimum.

325 Figure 6 shows the computed GCRs of protons energy spectra at the Earth for the last  
326 three solar minima with interplanetary parameters from observations shown in Table 1,  
327 which include the solar magnetic polarity, magnitude of IMF, SW speed, TA of HCS.  
328 As a reference, black solid line indicates the unmodulated GCR spectrum at the outer  
329 boundary. Lines shown in purple, black, and red colors represent  $P_{21/22}$ ,  $P_{22/23}$ , and  
330  $P_{23/24}$ , respectively. IMP-8 and STEREO spacecraft measurements of GCRs are shown  
331 as diamonds and squares, respectively, and red circles denote the measurements from  
332 PAMELA instrument in the higher energy range for the year 2009 [Adriani et al., 2013,  
333 Table 1]. For each energy point, the flux is calculated with a stochastic process simulation.  
334 From Figure 6 we can see that with diffusion parameters  $a = 0.03$ ,  $b = 0.02$ , and  $d = 0.5$ ,  
335 the simulation results fit well to the IMP-8 observational data during  $P_{21/22}$  and  $P_{22/23}$ .  
336 As discussed earlier, in the solar minimum  $P_{23/24}$  the solar activity was extremely quiet,  
337 so that the particles perpendicular diffusion coefficients are set to be smaller, and that the  
338 particles parallel diffusion coefficients are larger. For this reason, in  $P_{23/24}$  the parameters  
339  $a$  and  $b$  should be smaller and the parameter  $d$  should be larger. From Figure 6 it is shown  
340 that with parameters  $a = 0.02$ ,  $b = 0.01$ , and  $d = 1$ , and other parameters set as in Table  
341 1, the simulation results fit well to the observations from both STEREO and PAMELA  
342 during the solar minimum  $P_{23/24}$ .

343 Figure 7 shows a comparison of the integral intensity  $M(E)$  as a function of GCR  
 344 energy  $E$  between our simulation results and the NM measurements. Similar to Figure  
 345 6, the black solid line indicates the unmodulated GCR spectrum, and the three lines in  
 346 different colors represent our calculations for the three solar minima. Note that both  
 347 simulation result and observation of each solar minimum are multiplied by an arbitrary  
 348 factor for the purpose of presentation. For each NM with a cutoff rigidity  $P_c$  given in  
 349 Table 2, we have calculated  $M(E_{\text{eff}})$  (colored lines) as an integration of simulated GCR  
 350 flux  $j(E)$  using equation (13). In order to make a direct comparison between  $M(E_{\text{eff}})$   
 351 from our simulation results (green line) and the NM count rates in  $P_{21/22}$ , we obtain a  
 352 normalization constant  $K_{\text{NM}}$  with equation (14) for each NM, and we show the  $K_{\text{NM}}$  in  
 353 Table 2. With the  $K_{\text{NM}}$  we can convert all NMs' count rates  $N(P_c)$  to their  $M(E_{\text{NM}})$ ,  
 354 which is denoted as observational data (color dots) for periods other than  $P_{21/22}$ . Note  
 355 that the constants  $K_{\text{NM}}$  are obtained with equation (14) for data in  $P_{21/22}$ , so the green  
 356 dots agree with green line exactly for  $P_{21/22}$ . For the other two solar minima, we use the  
 357 same normalization constant and NM measurements to obtain the black and red dots,  
 358 which are considered as measurements. Therefore, the fact that the blue and red dots  
 359 agree well with black and red lines, respectively, show that our simulation results fit well  
 360 with the NMs count rates for periods  $P_{22/23}$  and  $P_{23/24}$ . We especially point out that  
 361 in  $P_{23/24}$ , the NMs count rates were much higher than previous solar minima and our  
 362 simulations reproduce such a phenomenon.

363 Furthermore, we study the evolution of the proton energy spectrum during the period  
 364 of the solar minimum  $P_{23/24}$  (Figure 8). The proton flux measurements from PAMELA  
 365 instrument with monthly average [Adriani et al., 2013, table 1] for year 2007, 2008 and

366 2009 are represented with purple, black and red circles respectively. Obviously, the proton  
367 spectra in 2009 represents the highest flux observed. Figure 8 also shows the computed  
368 differential intensity of GCR protons at the Earth from 2007 to 2009 (solid lines) in half-  
369 year periods. For simulations in these half-year periods, the SW speed, magnitude of  
370 IMF and TA of HCS are from the averaged observations, while the diffusion coefficient  
371 parameters  $a$ ,  $b$ , and  $d$  are the same as the  $P_{23/24}$  solar minimum. We can see that the  
372 simulation results agree well with PAMELA measurements.

## 8. Discussion

373 We investigate the behaviors of GCR modulation at Earth and try to determine the  
374 potential mechanisms responsible for the abnormally high GCR intensity in the last solar  
375 minimum. through comparing the numerical simulation results with the observations from  
376 NM stations and spacecraft.

377 Various modulation processes could contribute to the high GCR intensity, e.g., particle  
378 drifts, diffusion, or even possible weakened modulation by the heliosheath. Generally,  
379 drifts effects are thought to dominant modulation process at solar minimum for the  $A < 0$   
380 epochs [Kóta and Jokipii, 1983]. Cliver et al. [2013] argues that diffusion is the primary  
381 modulation process during this unusual solar minimum. Potgieter et al. [2014] also shows  
382 that the rigidity-dependent diffusion coefficients need to decrease significantly below  $\sim 3$   
383 GeV to reproduce the proton spectra from PAMELA experiment. In this work, we fur-  
384 ther stress that a possible low magnetic turbulence, which increases the parallel diffusion  
385 and reduces the perpendicular diffusion in the polar direction, might be an additional  
386 mechanism for the high GCR intensity during the  $P_{23/24}$  solar minimum.

387 Energetic particles can be scattered parallel to the background magnetic field because  
388 of magnetic turbulence, so higher turbulence levels could cause a stronger scattering or  
389 shorter parallel mean free path. Particle perpendicular diffusion is achieved with the  
390 motion particle gyrocenters caused by turbulence. Therefore, lower turbulence levels  
391 should increase parallel diffusion and decrease perpendicular diffusion [e.g., Jokipii, 1966;  
392 Matthaeus et al., 2003; Qin, 2007].

393 However, drifts still play a significant role in the modulation process, even though the  
394 2009 solar minimum is more ‘diffusion dominated’ than previous solar minima [Potgieter  
395 et al., 2014]. When the perpendicular diffusion is low, particles tends to stay with the cur-  
396 rent sheet longer, which brings GCR rapidly during the  $A < 0$  solar minimum. A low SW  
397 speed can cause less outward convection of GCRs out of the heliosphere and less adiabatic  
398 cooling, but a slow SW also causes magnetic field lines more tightly wound, slowing down  
399 GCR propagation. A low magnitude of IMF would cause increase of particle drift accord-  
400 ing to equation (8) in our model and diffusion. In fact, the more realistic scenario is that  
401 all modulation processes interplay dynamically, contributing to the observed increases in  
402 the proton spectra.

403 In this work, we assume ad hoc changes in the magnitude of diffusion coefficients.  
404 Although we can use some diffusion models with assumptions of magnetic turbulence  
405 type and its transport in the heliosphere[e.g., NLGC, Matthaeus et al., 2003]. This way  
406 may introduce many more free parameters.

407 There are several parameters that control the properties magnetic turbulence, such  
408 as turbulence levels and turbulence correlation scales, all of which are important to the  
409 diffusion coefficients. Nevertheless, since there is no direct measurement of diffusion co-

410 efficient, it is very difficult to estimate the diffusion coefficients in exact magnitude via  
411 comparing simulation results with the observations.

## 9. Conclusions

412 Observations of GCR count rates of NMs and the transport parameters from spacecraft  
413 measurements for the last three solar cycles show that during the solar minimum  $P_{23/24}$ ,  
414 the intensity of GCRs was the highest, while the IMF and the SW speed were both weaker  
415 than the previous two solar minima,  $P_{21/22}$  and  $P_{22/23}$ , but the TA of HCS was not at  
416 the lowest level. We first study how the modulation of GCR is related to these transport  
417 parameters, which include the SW speed, outer heliospheric boundary, magnitude of IMF  
418 at the Earth, and parallel and perpendicular diffusion coefficients. Despite the fact that  
419 drifts still play a significant role in the modulation process, we find that the TA of HCS  
420 during  $P_{23/24}$  is not small enough to explain the large increase of GCRs intensity. Particle  
421 drift cannot contribute solely to the high flux of GCRs in  $P_{23/24}$ . Furthermore, during the  
422 recent solar minimum  $P_{23/24}$ , the solar activity was very weak and solar wind turbulence  
423 level was expected to be lower than previous solar minima, so that particles radial and  
424 polar perpendicular diffusion coefficients should be smaller and parallel diffusion coeffi-  
425 cients should be larger. Therefore, we have to further tune the magnitude of diffusion  
426 coefficients. It is found that a lower polar perpendicular diffusion with factor  $b$  can cause  
427 the increase of GCRs intensity. In addition, the factor  $b$  is more effective than the radial  
428 perpendicular diffusion factor  $a$  and parallel diffusion factor  $d$  for the  $A < 0$  cycle. The  
429 combination of lower polar diffusion coefficient, higher parallel diffusion coefficient, lower  
430 SW speed, and lower magnetic field in the solar minimum  $P_{23/24}$  is possible to explain the  
431 unusually high GCR intensity.

432 Although relatively simple models are implemented in our simulation model, this work  
433 represents an important first step towards investigating the unusual cosmic ray modulation  
434 during the last solar minimum quantitatively. Further effort is needed to overcome these  
435 limitations in a more comprehensive way.

436 **Acknowledgments.** This work was supported in part by grants NNSFC 41125016,  
437 NNSFC 41374177, CMA grant GYHY201106011, and the Specialized Research Fund for  
438 State Key Laboratories of China. The computations were performed by Numerical Fore-  
439 cast Modeling R&D and VR System of State Key Laboratory of Space Weather and  
440 Special HPC work stand of Chinese Meridian Project. We benefited from the Sunspot  
441 data provided by SIDC Team 2009, the Wilcox Solar Observatory data obtained via the  
442 web site <http://wso.stanford.edu>, energetic particle data provided by IMP-8 Goddard  
443 Medium Energy (GME) Experiment, STEREO High Energy Telescope (HET). We are  
444 grateful to the SPDF OMNIWeb interface at <http://omniweb.gsfc.nasa.gov> for the solar  
445 and interplanetary data. We also thank the providers of NM data used in this study.

## References

- 446 Adriani, O., et al. (2011), PAMELA measurements of cosmic-ray proton and helium  
447 spectra, *Science*, *332*(6025), 69–72, doi:10.1126/science.1199172.
- 448 Adriani, O., et al. (2013), Time eependence of the proton flux measured by PAMELA  
449 during the 2006 July-2009 December solar minimum, *Astrophys. J.*, *765*, 91, doi:  
450 10.1088/0004-637X/765/2/91.
- 451 Ahluwalia, H. S., and M. M. Fikani (2007), Cosmic ray detector response to tran-  
452 sient solar modulation: Forbush decreases, *J. Geophys. Res.*, *112*, A08105, doi:

- 453 10.1029/2006JA011958.
- 454 Ahluwalia, H. S., C. Lopate, R. C. Ygbuhay, and M. L. Duldig (2010), Galactic cos-  
455 mic ray modulation for sunspot cycle 23, *Adv. Space Res.*, *46*(7), 934 – 941, doi:  
456 <http://dx.doi.org/10.1016/j.asr.2010.04.008>.
- 457 Ahluwalia, H. S., M. V. Alania, A. Wawrzynczak, R. C. Ygbuhay, and M. M. Fikani  
458 (2013), May 2005 halo cmes and galactic cosmic ray flux changes at earths orbit, *Solar*  
459 *Phys.*, pp. 1–20, doi:10.1007/s11207-013-0439-9.
- 460 Alanko, K., I. G. Usoskin, K. Mursula, and G. A. Kovaltsov (2003), Heliospheric mod-  
461 ulation strength: effective neutron monitor energy, *Adv. Space Res.*, *32*(4), 615–620,  
462 doi:10.1016/S0273-1177(03)00348-X.
- 463 Ball, B., M. Zhang, H. Rassoul, and T. Linde (2005), Galactic cosmic-ray modulation  
464 using a solar minimum MHD heliosphere: a stochastic particle approach, *Astrophys. J.*,  
465 *634*(2), 1116, doi:10.1086/496965.
- 466 Burger, R. A. (2012), Modeling drift along the heliospheric wavy neutral sheet, *Astrophys.*  
467 *J.*, *760*(1), 60, doi:10.1088/0004-637X/760/1/60.
- 468 Burger, R. A., and M. S. Potgieter (1989), The calculation of neutral sheet drift in  
469 two-dimensional cosmic-ray modulation models, *Astrophys. J.*, *339*, 501–511, doi:  
470 10.1086/167313.
- 471 Büsching, I., and M. S. Potgieter (2008), The variability of the proton cosmic ray flux  
472 on the Sun’s way around the galactic center, *Adv. Space Res.*, *42*, 504–509, doi:  
473 10.1016/j.asr.2007.05.051.
- 474 Caballero-Lopez, R. A., and H. Moraal (2004), Limitations of the force field equa-  
475 tion to describe cosmic ray modulation, *J. Geophys. Res.*, *109*, A01101, doi:

476 10.1029/2003JA010098.

477 Cliver, E. W., I. G. Richardson, and A. G. Ling (2013), Solar Drivers of 11-yr and Long-  
478 Term Cosmic Ray Modulation, *Space Sci. Rev.*, *176*, 3–19, doi:10.1007/s11214-011-9746-  
479 3.

480 Decker, R. B., S. M. Krimigis, E. C. Roelof, and M. E. Hill (2012), No merid-  
481 ional plasma flow in the heliosheath transition region, *Nature*, *489*, 124–127, doi:  
482 10.1038/nature11441.

483 Effenberger, F., H. Fichtner, K. Scherer, S. Barra, J. Kleimann, and R. D. Strauss (2012a),  
484 A generalized diffusion tensor for fully anisotropic diffusion of energetic particles in the  
485 heliospheric magnetic field, *Astrophys. J.*, *750*, 108, doi:10.1088/0004-637X/750/2/108.

486 Effenberger, F., H. Fichtner, K. Scherer, and I. Büsching (2012b), Anisotropic diffusion  
487 of galactic cosmic ray protons and their steady-state azimuthal distribution, *Astrophys.*  
488 *J.*, *547*, A120, doi:10.1051/0004-6361/201220203.

489 Ferreira, S. E. S., M. S. Potgieter, R. A. Burger, B. Heber, and H. Fichtner (2001), Mod-  
490 ulation of Jovian and galactic electrons in the heliosphere: 1. Latitudinal transport of a  
491 few MeV electrons, *J. Geophys. Res.*, *106*, 24,979–24,988, doi:10.1029/2001JA000082.

492 Giacalone, J., and J. R. Jokipii (1999), The transport of cosmic rays across a turbulent  
493 magnetic field, *Astrophys. J.*, *520*, 204–214, doi:10.1086/307452.

494 Goring, D., and V. Nikora (2002), Despiking acoustic doppler velocimeter data, *J. Hy-*  
495 *draul. Eng.*, *128*(1), 117–126, doi:10.1061/(ASCE)0733-9429(2002)128:1(117).

496 Heber, B., H. Fichtner, and K. Scherer (2006), Solar and heliospheric modulation of  
497 galactic cosmic rays, *Space Sci. Rev.*, *125*, 81–93, doi:10.1007/s11214-006-9048-3.

- 498 Heber, B., A. Kopp, J. Gieseler, R. Müller-Mellin, H. Fichtner, K. Scherer, M. S. Potgieter,  
499 and S. E. S. Ferreira (2009), Modulation of galactic cosmic ray protons and electrons  
500 during an unusual solar minimum, *Astrophys. J.*, *699*, 1956–1963, doi:10.1088/0004-  
501 637X/699/2/1956.
- 502 Herbst, K., A. Kopp, B. Heber, F. Steinhilber, H. Fichtner, K. Scherer, and D. Matthiä  
503 (2010), On the importance of the local interstellar spectrum for the solar modulation  
504 parameter, *J. Geophys. Res.*, *115*, D00I20, doi:10.1029/2009JD012557.
- 505 Herbst, K., B. Heber, A. Kopp, O. Sternal, and F. Steinhilber (2012), The local inter-  
506 stellar spectrum beyond the heliopause: what can be learned from Voyager in the inner  
507 heliosheath?, *Astrophys. J.*, *761*, 17, doi:10.1088/0004-637X/761/1/17.
- 508 Hitge, M., and R. A. Burger (2010), Cosmic ray modulation with a Fisk-type heliospheric  
509 magnetic field and a latitude-dependent solar wind speed, *Adv. Space Res.*, *45*, 18–27,  
510 doi:10.1016/j.asr.2009.07.024.
- 511 Jokipii, J. R. (1966), Cosmic-ray propagation. I. charged particles in a random magnetic  
512 field, *Astrophys. J.*, *146*, 480, doi:10.1086/148912.
- 513 Jokipii, J. R., and D. A. Kopriva (1979), Effects of particle drift on the transport of  
514 cosmic rays. III - Numerical models of galactic cosmic-ray modulation, *Astrophys. J.*,  
515 *234*, 384–392, doi:10.1086/157506.
- 516 Jokipii, J. R., and J. Kóta (2000), Galactic and anomalous cosmic rays in the heliosphere,  
517 *Astrophys. Space Sci.*, *274*, 77–96, doi:10.1023/A:1026535603934.
- 518 Jokipii, J. R., and B. Thomas (1981), Effects of drift on the transport of cosmic rays. IV  
519 - Modulation by a wavy interplanetary current sheet, *Astrophys. J.*, *243*, 1115–1122,  
520 doi:10.1086/158675.

- 521 Kopp, A., I. Büsching, R. D. Strauss, and M. S. Potgieter (2012), A stochastic differen-  
522 tial equation code for multidimensional Fokker-Planck type problems, *Comput. Phys.*  
523 *Commun.*, *183*, 530–542, doi:10.1016/j.cpc.2011.11.014.
- 524 Kóta, J. (2013), Theory and modeling of galactic cosmic rays: trends and prospects,  
525 *Space. Sci. Rev.*, *176*, 391–403, doi:10.1007/s11214-012-9870-8.
- 526 Kóta, J., and J. R. Jokipii (1983), Effects of drift on the transport of cosmic rays.  
527 VI - a three-dimensional model including diffusion, *Astrophys. J.*, *265*, 573–581, doi:  
528 10.1086/160701.
- 529 Manuel, R., S. E. S. Ferreira, M. S. Potgieter, R. D. Strauss, and N. E. Engelbrecht  
530 (2011), Time-dependent cosmic ray modulation, *Adv. Space Res.*, *47*(9), 1529 – 1537,  
531 doi:10.1016/j.asr.2010.12.007.
- 532 Matthaeus, W. H., G. Qin, J. W. Bieber, and G. P. Zank (2003), Nonlinear collision-  
533 less perpendicular diffusion of charged particles, *Astrophys. J.*, *590*, L53–L56, doi:  
534 10.1086/376613.
- 535 McDonald, F. B. (1998), Cosmic-ray modulation in the heliosphere—a phenomenological  
536 study, *Space Sci. Rev.*, *83*, 33–50, doi:10.1023/A:1005052908493.
- 537 Moraal, H. (2013), Cosmic-Ray Modulation Equations, *Space Sci. Rev.*, *176*, 299–319,  
538 doi:10.1007/s11214-011-9819-3.
- 539 Nymmik, R. A., M. I. Panasyuk, T. I. Pervaja, and A. A. Suslov (1992), A model of  
540 galactic cosmic ray fluxes, *Int. J. Rad. Appl. Instrum. Part D. Nucl. Track. Radiat.*  
541 *Meas.*, *20*(3), 427–429, doi:http://dx.doi.org/10.1016/1359-0189(92)90028-T.
- 542 Parker, E. N. (1965), The passage of energetic charged particles through interplanetary  
543 space, *Planet. Space Sci.*, *13*, 9–49, doi:10.1016/0032-0633(65)90131-5.

- 544 Pei, C., J. W. Bieber, R. A. Burger, and J. Clem (2010), A general time-dependent  
545 stochastic method for solving parker’s transport equation in spherical coordinates, *J.*  
546 *Geophys. Res.*, *115*(A12), A12,107.
- 547 Pogorelov, N. V., J. Heerikhuisen, G. P. Zank, and S. N. Borovikov (2009), Influence of  
548 the interstellar magnetic field and neutrals on the shape of the outer heliosphere, *Space*  
549 *Sci. Rev.*, *143*, 31–42, doi:10.1007/s11214-008-9429-x.
- 550 Potgieter, M. (2013), Solar modulation of cosmic rays, *Living Rev. Solar Phys.*, *10*, 3,  
551 doi:10.12942/lrsp-2013-3.
- 552 Potgieter, M. S. (1998), The modulation of galactic cosmic rays in the heliosphere: theory  
553 and models, *Space Sci. Rev.*, *83*(1), 147–158, doi:10.1023/A:1005014722123.
- 554 Potgieter, M. S., E. E. Vos, M. Boezio, N. De Simone, V. Di Felice, and V. Formato  
555 (2014), Modulation of Galactic Protons in the Heliosphere During the Unusual Solar  
556 Minimum of 2006 to 2009, *Solar Phys.*, *289*, 391–406, doi:10.1007/s11207-013-0324-6.
- 557 Qin, G. (2002), Charged particle transport in magnetic field turbulence and study of trim  
558 simulation and SSX experiment, Ph.D. thesis, University of Delaware.
- 559 Qin, G. (2007), Nonlinear parallel diffusion of charged particles: extension to the nonlinear  
560 guiding center theory, *Astrophys. J.*, *656*, 217–221, doi:10.1086/510510.
- 561 Qin, G., M. Zhang, J. R. Dwyer, and H. K. Rassoul (2004), Interplanetary transport mech-  
562 anisms of solar energetic particles, *Astrophys. J.*, *609*, 1076–1081, doi:10.1086/421101.
- 563 Qin, G., M. Zhang, J. R. Dwyer, H. K. Rassoul, and G. M. Mason (2005), The model  
564 dependence of solar energetic particle mean free paths under weak scattering, *Astrophys.*  
565 *J.*, *627*, 562–566, doi:10.1086/430136.

566 Qin, G., L.-L. Zhao, and H.-C. Chen (2012), Despiking of spacecraft energetic proton flux  
567 to study galactic cosmic-ray modulation, *Astrophys. J.*, *752*(2), 138, doi:10.1088/0004-  
568 637X/752/2/138.

569 Reinecke, J. P. L., and M. S. Potgieter (1993), An explanation for the observed intersection  
570 of cosmic-ray spectra for consecutive solar minimum periods, *Int. Cosmic Ray Conf.*,  
571 *3*, 597.

572 Scherer, K., and H. J. Fahr (2003), Solar cycle induced variations of the outer heliospheric  
573 structures, *Geophys. Res. Lett.*, *30*(2), 1045, doi:10.1029/2002GL016073.

574 Scherer, K., H.-J. Fahr, H. Fichtner, and B. Heber (2004), Long-term modulation of  
575 cosmic rays in the heliosphere and its influence at earth, *Solar Phys.*, *224*, 305–316,  
576 doi:10.1007/s11207-005-5687-x.

577 Scherer, K., H. Fichtner, R. D. Strauss, S. E. S. Ferreira, M. S. Potgieter, and H.-J. Fahr  
578 (2011), On cosmic ray modulation beyond the heliopause: where is the modulation  
579 boundary?, *Astrophys. J.*, *735*, 128, doi:10.1088/0004-637X/735/2/128.

580 Shalchi, A., and I. Büsching (2010), Influence of turbulence dissipation effects on the  
581 propagation of low-energy cosmic rays in the galaxy, *Astrophys. J.*, *725*, 2110–2116,  
582 doi:10.1088/0004-637X/725/2/2110.

583 Shalchi, A., J. W. Bieber, and W. H. Matthaeus (2004), Analytic forms of the perpen-  
584 dicular diffusion coefficient in magnetostatic turbulence, *Astrophys. J.*, *604*, 675–686,  
585 doi:10.1086/382128.

586 Strauss, R. D., and M. S. Potgieter (2014), Where does the helio-  
587 spheric modulation of galactic cosmic rays start?, *Adv. Space Res.*, doi:  
588 <http://dx.doi.org/10.1016/j.asr.2014.01.004>.

- 589 Strauss, R. D., M. S. Potgieter, A. Kopp, and I. Büsching (2011), On the propagation  
590 times and energy losses of cosmic rays in the heliosphere, *J. Geophys. Res.*, *116*, A12105,  
591 doi:10.1029/2011JA016831.
- 592 Strauss, R. D., M. S. Potgieter, I. Büsching, and A. Kopp (2012), Modelling heliospheric  
593 current sheet drift in stochastic cosmic ray transport models, *Astrophys. Space Sci.*,  
594 *339*, 223–236, doi:10.1007/s10509-012-1003-z.
- 595 Strauss, R. D., M. S. Potgieter, S. E. S. Ferreira, H. Fichtner, and K. Scherer (2013),  
596 Cosmic ray modulation beyond the heliopause: a hybrid modeling approach, *Astrophys.*  
597 *J. Lett.*, *765*, L18, doi:10.1088/2041-8205/765/1/L18.
- 598 Webber, W. R., P. R. Higbie, and F. B. McDonald (2013), The unfolding of the spectra  
599 of low energy galactic cosmic ray H and He nuclei as the Voyager 1 spacecraft exits the  
600 region of heliospheric modulation, *ArXiv e-prints*.
- 601 Zank, G. P., and H.-R. Müller (2003), The dynamical heliosphere, *J. Geophys. Res.*, *108*,  
602 1240, doi:10.1029/2002JA009689.
- 603 Zank, G. P., G. Li, V. Florinski, W. H. Matthaeus, G. M. Webb, and J. A. Le Roux  
604 (2004), Perpendicular diffusion coefficient for charged particles of arbitrary energy, *J.*  
605 *Geophys. Res.*, *109*, A04107, doi:10.1029/2003JA010301.
- 606 Zhang, M. (1999), A markov stochastic process theory of cosmic-ray modulation, *Astro-*  
607 *phys. J.*, *513*, 409–420, doi:10.1086/306857.
- 608 Zhao, L.-L., and G. Qin (2013), An observation-based GCR model of heavy nuclei: mea-  
609 surements from CRIS onboard ACE spacecraft, *J. Geophys. Res.*, pp. 1837–1848, doi:  
610 10.1002/jgra.50235.

**Table 1.** Values of parameters used in the simulations for the last three solar minima.

Parameter	$P_{21/22}$	$P_{22/23}$	$P_{23/24}$
$A$	$< 0$	$> 0$	$< 0$
$V_{sw}$	442 km/s	416 km/s	360 km/s
$B_e$	5.5 nT	4.9 nT	3.9 nT
$\alpha$	$4.3^\circ$	$4.3^\circ$	$6.3^\circ$
$a$	0.03	0.03	0.02
$b$	0.02	0.02	0.01
$d$	0.5	0.5	1

**Table 2.** Neutron Monitors(NMs) and parameters used in the comparison for the last three solar minima.

NM	$P_c$ (GV)	$E_{\text{eff}}$ (GeV)	$K_{\text{NM}}$ ( $\text{m}^{-2}\text{sr}^{-1}\text{GeV}^{-1}$ )
Apatity	0.65	6.50	$3.16 \times 10^{-5}$
Oulu	0.80	6.54	$3.53 \times 10^{-5}$
Yakutsk	1.65	6.87	$3.43 \times 10^{-5}$
Moscow	2.43	7.41	$2.07 \times 10^{-5}$
Novosibirsk	2.91	7.89	$3.43 \times 10^{-5}$
Lomnický Stit	3.98	9.46	$8.72 \times 10^{-5}$
Jungfraujoch	4.49	10.47	$2.05 \times 10^{-5}$
Hermanus	4.58	10.67	$2.63 \times 10^{-5}$
Rome	6.32	15.59	$1.44 \times 10^{-5}$
Tbilisi	6.73	16.99	$6.78 \times 10^{-5}$
Potchefstroom	7.00	17.96	$2.69 \times 10^{-5}$

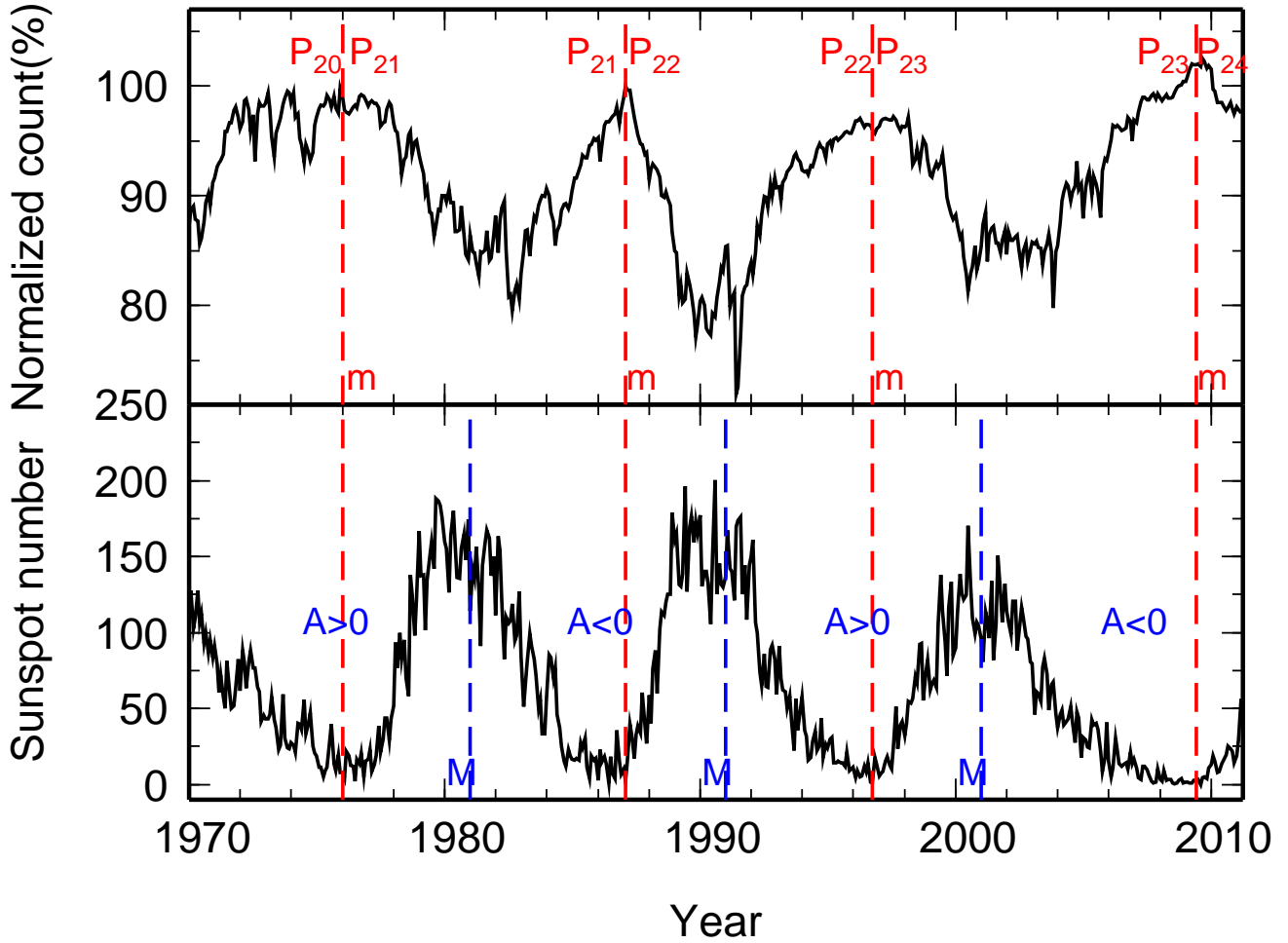


**Figure 1.** GCR intensity as measured by Apatity NM (upper panel) and monthly averaged SSN (lower panel). The red dashed-lines indicate the epochs of solar minima, and the red numbers represent solar cycles. The black dashed-lines indicate the epochs of solar maxima, and ‘ $A > 0$ ’ or ‘ $A < 0$ ’ represent the periods of solar magnetic polarity.

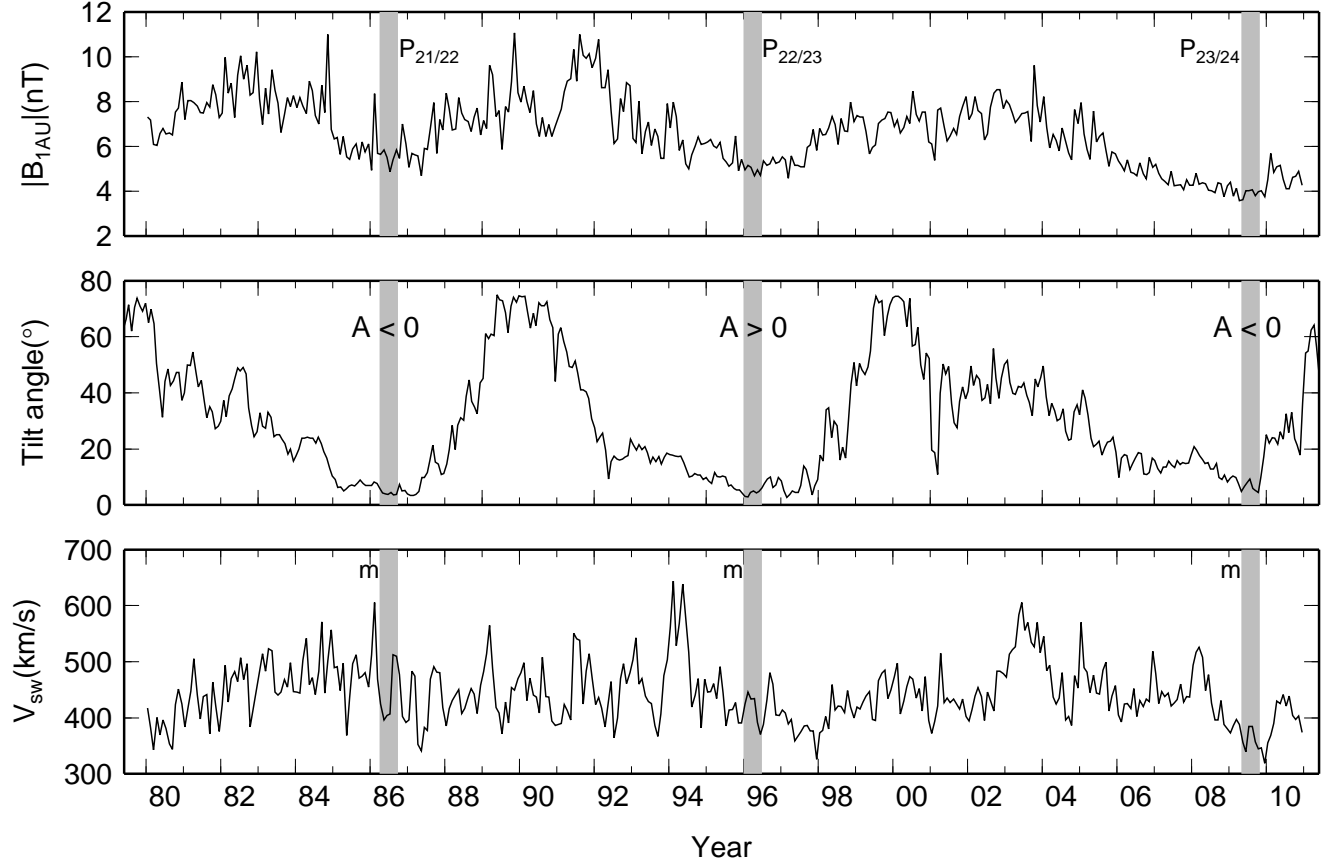


**Figure 2.** Temporal evolution interplanetary solar wind and magnetic field parameters measured at 1 AU. The IMF and SW speed are obtained by averaging the OMNI data over one-month intervals. The TA of the HCS is obtained from the WSO Web site with “new” model. The three grey shadow areas labeled with  $P_{21/22}$ ,  $P_{22/23}$  and  $P_{23/24}$  indicate the three (21/22, 22/23, and 23/24) epochs of the solar minimum of approximately half a year long.

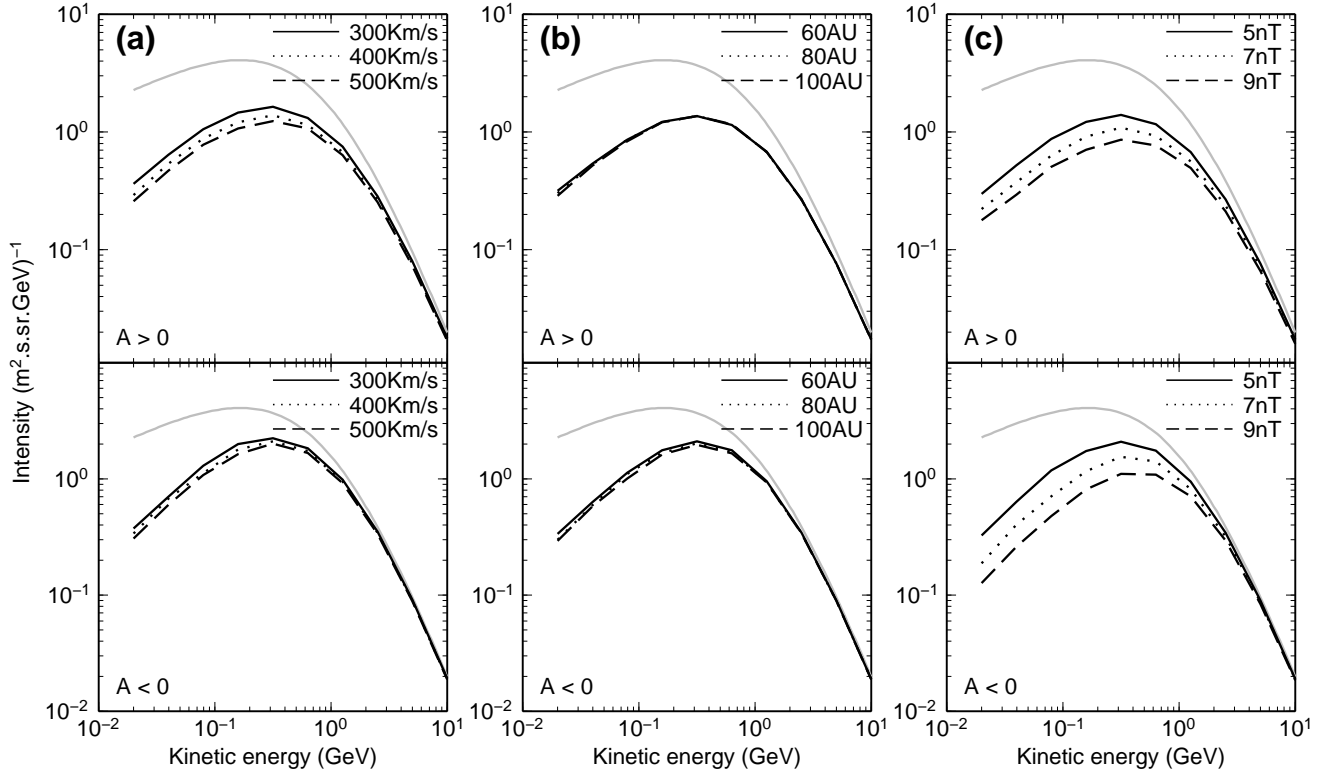


**Figure 3.** Computed differential intensity of GCR proton at Earth as a function of kinetic energy for both  $A > 0$  and  $A < 0$  magnetic polarities during the solar minimum condition with an unmodulated interstellar spectrum shown in grey line as a reference. Three different black lines indicate three assumptions for (a) SW speed, (b) distance of the outer heliospheric boundary, and (c) magnitude of IMF.

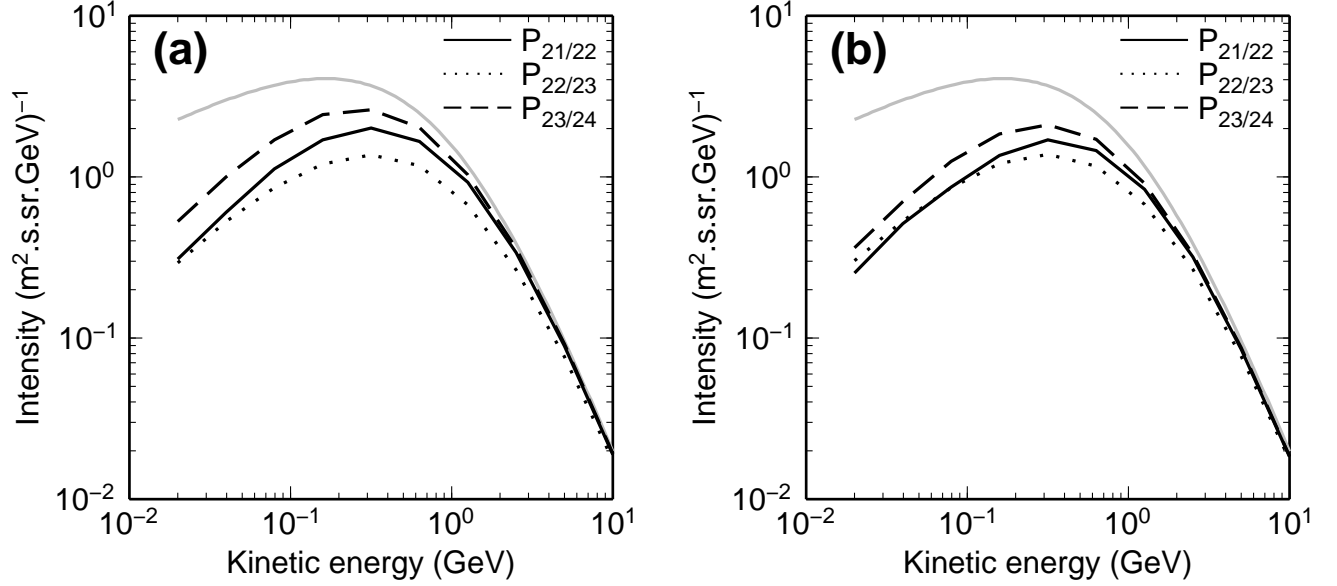


**Figure 4.** Computed GCR proton energy spectra at the Earth for different magnetic field strength  $B_e$  at Earth and SW speed  $V_{sw}$  with unmodulated interstellar spectrum shown in grey lines as a reference, during  $P_{21/22}$  (dark solid line),  $P_{22/23}$  (dotted line), and  $P_{23/24}$  (dashed line). The TA of HCS is set to be (a)  $0^\circ$  and (b) the measured values during the corresponding periods.

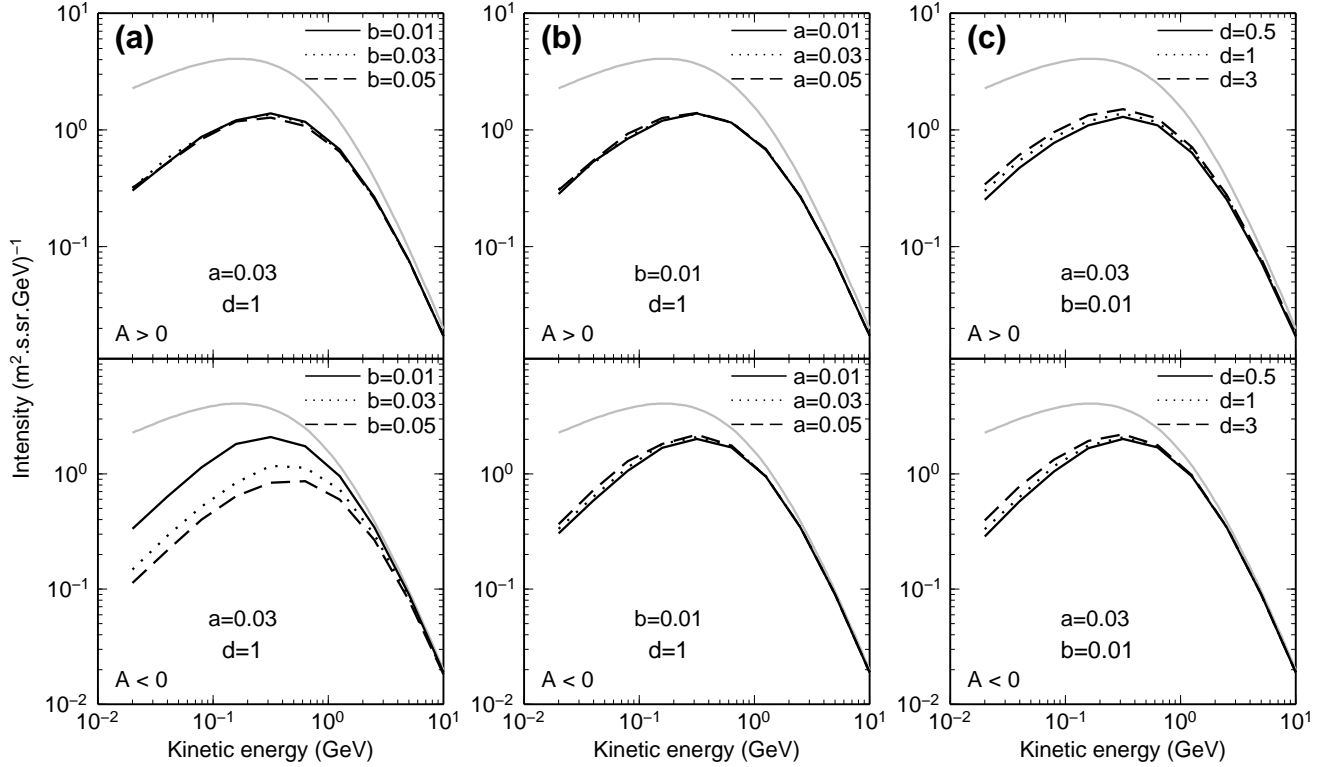


**Figure 5.** Computed differential intensity of GCR proton at Earth as a function of kinetic energy for both magnetic polarities during a solar minimum condition with unmodulated interstellar spectrum shown in grey lines as a reference. Three different black lines indicate three assumptions for (a) polar perpendicular diffusion factor  $b$ , (b) radial perpendicular diffusion factor  $a$  and (c) parallel diffusion factor  $d$ .

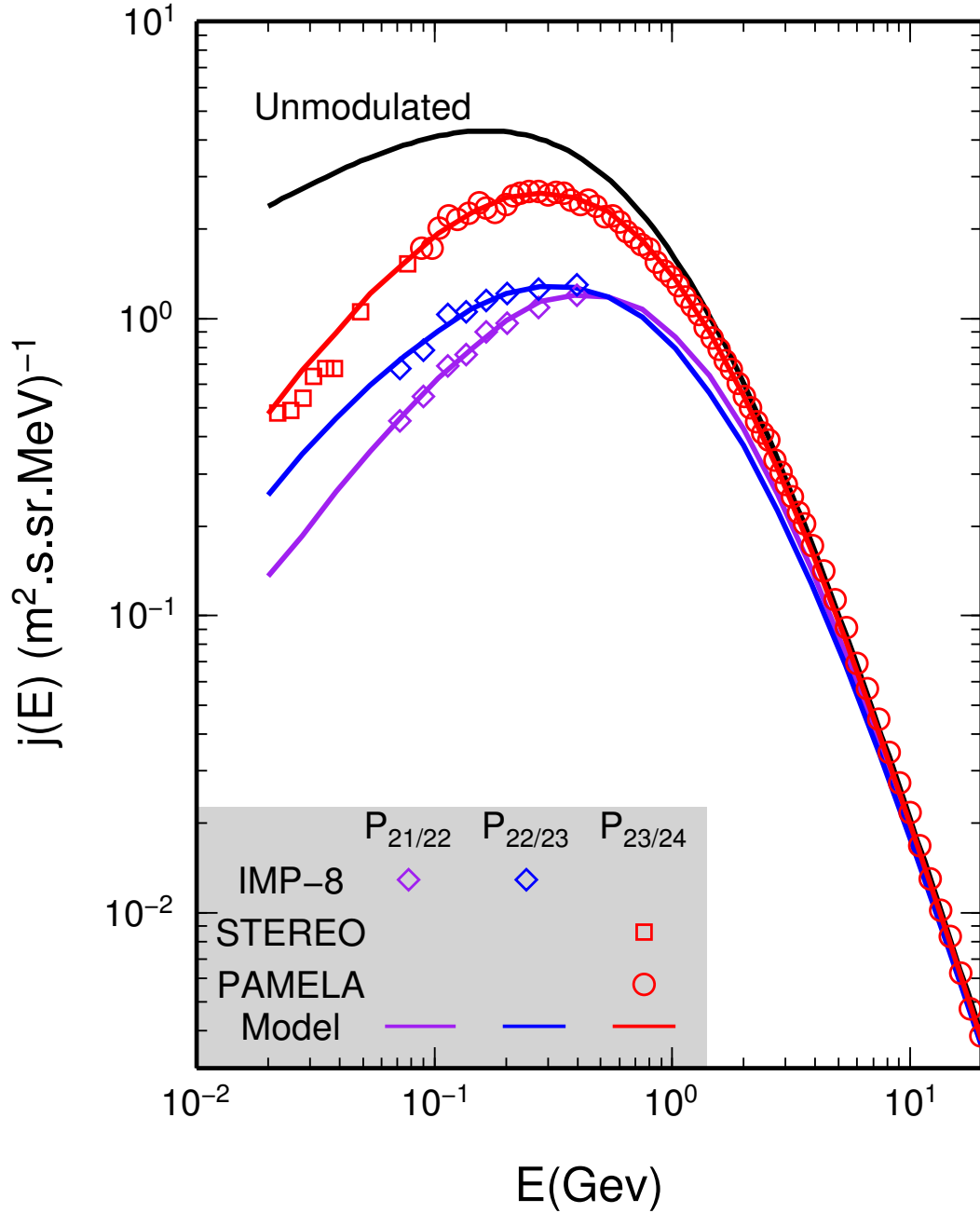


**Figure 6.** Computed GCR proton energy spectra at the Earth for the last three solar minima with parameters presented in table 1. The observation data are calculated from the measurements of proton flux by STEREO (squares) and IMP-8 (diamonds) after SEP contribution is removed. And red circles denote the measurements from PAMELA instrument for the year 2009 [Adriani et al., 2013, table 1].

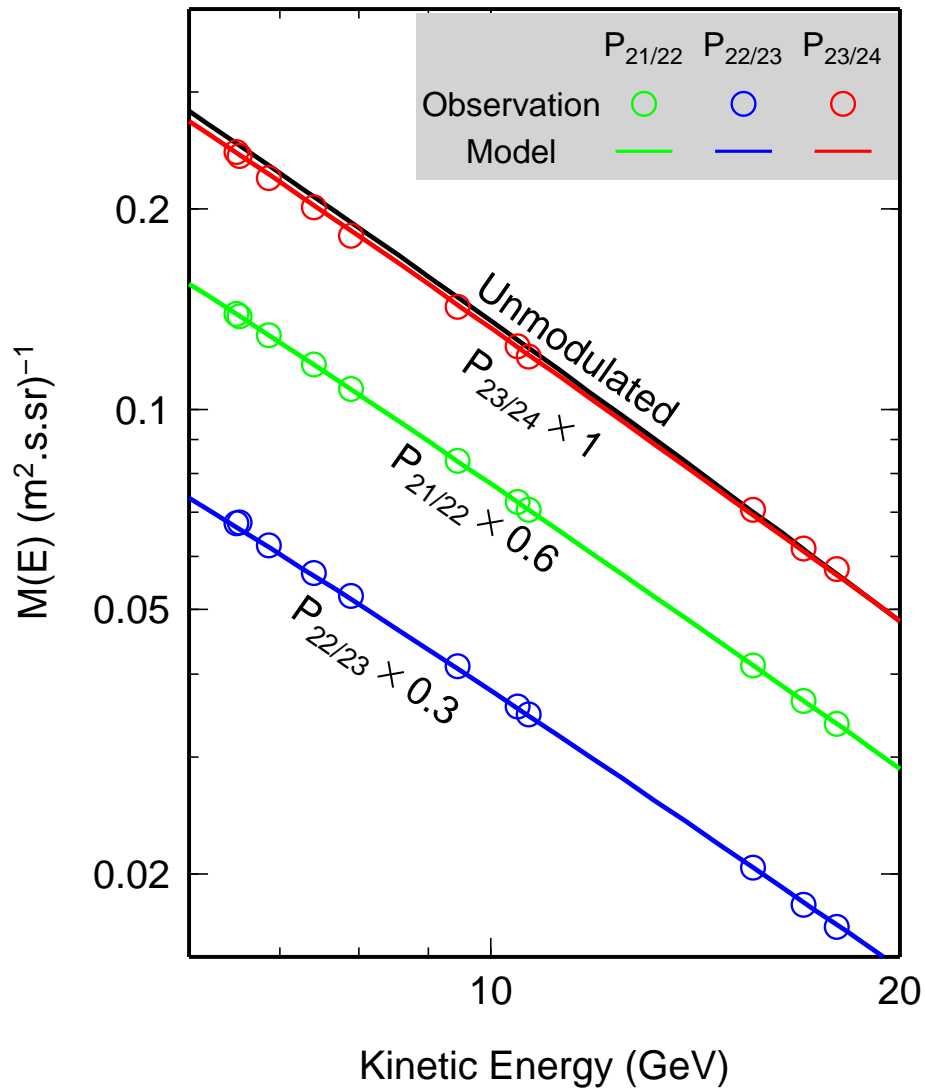


**Figure 7.** Comparison between the computed GCR integral flux and the NM count rates for the last three solar minima. Note that both simulation result and observation of each solar minimum are multiplied by an arbitrary factor as denoted in figure, for the purpose of presentation.

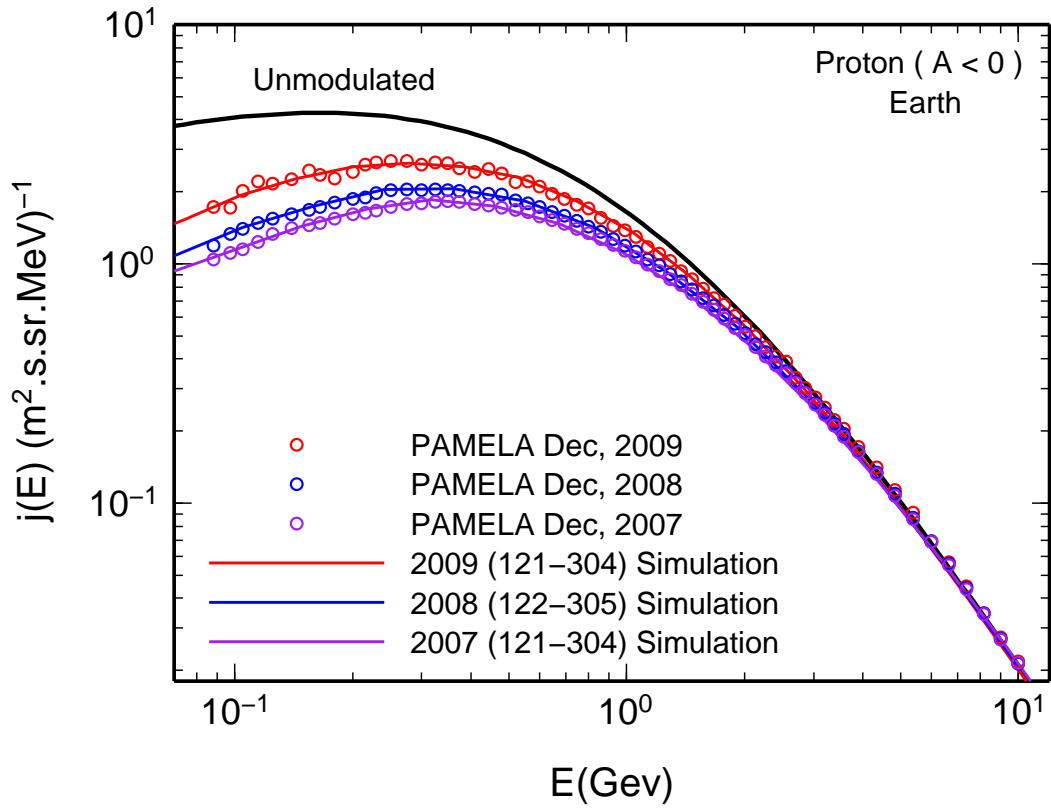


**Figure 8.** Evolution of the proton energy spectrum during the period of minimum solar activity, from year 2007 to year 2009. The purple, black and red curves indicate the computed GCR proton differential fluxes corresponding to three half-year periods, 2007 (121-304), 2008 (122-305), and 2009 (121-304), respectively. An unmodulated interstellar spectrum is shown in black line for reference. The observations from PAMELA instrument are also shown (circles).